Water Research X 19 (2023) 100182

Contents lists available at ScienceDirect

Water Research X

journal homepage: www.sciencedirect.com/journal/water-research-x

Boosted brackish water desalination and water softening by facilely designed MnO_2/hierarchical porous carbon as capacitive deionization electrode

Guangcai Tan, Shun Wan, Shu-Chuan Mei, Bo Gong, Chen Qian, Jie-Jie Chen *

CAS Key Laboratory of Urban Pollutant Conversion, Department of Environmental Science and Engineering, University of Science and Technology of China, Hefei 230026, China

ARTICLE INFO

Keywords:
Hierarchical porous carbon
Manganese dioxides
Brackish water desalination
Divalent cation selectivity
Multiscale simulation

ABSTRACT

Capacitive deionization (CDI) is a promising technique for brackish water desalination. However, its salt electrosorption capacity is insufficient for practical application yet, and little information is available on hardness ion (Mg^{2+}, Ca^{2+}) removal in CDI. Herein, hierarchical porous carbon (HPC) was prepared from low-cost and renewable microalgae via a simple one-pot approach, and both MnO_2/HPC and polyaniline/HPC (PANI/HPC) composites were then synthesized using a facile, one-step hydrothermal method. Compared with the MnO_2 electrode, the MnO_2/HPC electrode presented an improved hydrophilicity, higher specific capacitance, and lower electrode resistance. The electrodes exhibited pseudocapacitive behaviors, and the maximum salt electrosorption capacities of MnO_2/HPC-PANI/HPC CDI cell was up to 0.65 mmol g^{-1} NaCl, 0.71 mmol g^{-1} $MgCl_2$, and 0.76 mmol g^{-1} $CaCl_2$, respectively, which were comparable and even higher than those of the previously reported CDI cells. Additionally, the MnO_2/HPC electrode presented a selectivity order of $Ca^{2+} \geq Mg^{2+} > Na^{+}$, and the divalent cation selectivity was found to be attributed to their stronger binding strength in the cavity of MnO_2. Multiscale simulations further reveal that the MnO_2/HPC electrodes with the unique luminal configuration of MnO_2 and HPC as supportive framework could offer a great intercalation selectivity of the divalent cations and exhibit a great promise in hardness ion removal.

1. Introduction

Desalination has been widely applied to tackle the escalating freshwater scarcity. Currently, there are two main types of water desalination technologies: reverse osmosis and thermal distillation (Caldera and Breyer, 2023). However, the energy consumption of reverse osmosis is high, and membrane fouling at high pressure is another problem that needs to be resolved. Thermal distillation consumes even more thermal and electric energy to vapor water, which makes it very expensive and results in a large emission of greenhouse gasses (Srimuk et al., 2020). In addition, water hardness is a problem broadly existing in tap, river, and ground water. This is mainly owning to the presence of calcium (Ca^{2+}) and magnesium (Mg^{2+}) ions, which can induce scaling problems in heat exchangers, pipelines of boilers, and electrical appliances (He et al., 2018; Zhang et al., 2020). Several approaches including ion exchange, chemical precipitation, nanofiltration, reverse osmosis, and electrodialysis have been applied for water softening (Zhang et al., 2020). However, these processes either consume a large amount of energy or require an excessive use of chemicals. Thus, the development of an environmentally friendly and low energy consuming technology is highly desirable for brackish water desalination and water softening.

Capacitive deionization (CDI) is an electrochemically controlled method based on electrosorption of ions through the formation of an electric double layer (EDL) on the surface of two porous carbon electrodes (Bhat et al., 2019). Due to its environmentally friendly, low-cost, and high-energy-efficiency features, CDI has emerged as a promising desalination technology for brackish water treatment (Oyarzun et al., 2018; Zhang et al., 2021). Nevertheless, the undesirable expulsion of the co-ions in the carbon electrode will lead to a lower salt electrosorption capacity and higher energy consumption (Gamaethiralalage et al., 2021; Tan et al., 2020). In order to improve the salt electrosorption capacity, redox-active and pseudocapacitive materials such as $Na_3V_2(PO_4)_3$, CuHCF and MnO_2 have been employed as CDI electrodes (Srimuk et al., 2020). However, these materials always suffer from poor conductivity

* Corresponding author.
E-mail address: chenjiej@ustc.edu.cn (J.-J. Chen).

https://doi.org/10.1016/j.wroa.2023.100182
Received 8 March 2023; Received in revised form 30 April 2023; Accepted 9 May 2023
Available online 10 May 2023

and/or volume expansion-contraction in the ion intercalation/deintercalation process, which can result in poor cycling stability (Chen et al., 2013; Wang et al., 2019). Thus, designing composite materials composed of carbon material with pseudocapacitive material (i.e., MnO_2) could be an efficient way to enhance electrical conductivity while mitigating the volume expansion-contraction, thereby enhancing desalination performance (Jia et al., 2018).

Hierarchical porous carbon (HPC) has a high surface area with a multimodal pore size distribution and can serve as a conductive network and buffer the volume expansion of the active material in battery and supercapacitor applications (Sevilla et al., 2017; Wang et al., 2017). In particular, renewable biomass, such as microalgae, can be utilized to synthesize HPC through a simple and sustainable one-pot approach (Sevilla et al., 2017). Compared to traditional materials, biomass-derived materials have demonstrated lower production costs and reduced energy consumption in certain applications (Hussain et al., 2021; Oliveira et al., 2021). Furthermore, studies have shown that biomass production can be scaled up using established methods and technologies, making it a viable option for large-scale applications (Oliveira et al., 2021). In addition, microalgae have extraordinary biomass productivity and a fast growth rate and can even be easily cultivated in nutrient-rich wastewaters. The unit CO_2 fixation capacity of microalgae is nearly 50 times higher than terrestrial plants (Zhou et al., 2017), production of HPC from microalgae could further accelerate CO_2 mitigation. More importantly, the uniform micron-sized cell bodies in microalgae can result in the production of carbon materials with large surface areas and controllable multimodal porosity (Rizwan et al., 2018). Thus, HPC derived from microalgae could be a great candidate as a supportive backbone in electrode materials for improving CDI performance. Various MnO_2 polymorphs (α, β and δ) have been used as electrode materials in CDI just for NaCl removal, owing to their environmentally friendly, low-cost, and high theoretical specific capacitance features (Leong and Yang 2019; Srimuk et al., 2020). Among them, α-MnO_2 with a large tunnel structure (4.6 × 4.6 Å) has been applied in multivalent ion batteries (including Mg, Ca and Al) as well (Juran et al., 2018). The square 2 × 2 loose tunnels are suitable for the insertion/extraction of ions with a large hydrated radius, suggesting that α-MnO_2 can be an efficient pseudocapacitive electrode in CDI for water softening. Therefore, integrating α-MnO_2 into the HPC surface will counteract their drawbacks and derive a synergistically improved hybrid electrode for CDI applications. In addition, although some carbon or battery electrodes have been used for divalent ions removal (Cerón et al., 2020; Chen et al., 2022; Singh et al., 2020; Shocron et al., 2022; Uwayid et al., 2022; Zhao et al., 2012), information regarding the use of hybrid electrodes for water softening and divalent cation selectivity in CDI systems remains limited.

Therefore, in this work, microalgae were used to prepare HPC first. Then, the α-MnO_2 nanorods were uniformly dispersed on the HPC surface, and PANI was grafted on HPC via a facile, one-step hydrothermal procedure. Later, the brackish water desalination and water softening performance of the prepared MnO_2/HPC-PANI/HPC CDI cell was evaluated. In addition, the MnO_2/HPC electrode was used to evaluate the competitive intercalation between Na^+, Mg^{2+} and Ca^{2+} in the binary salt solutions. Furthermore, the underlying mechanisms for cation selectivity were elucidated using molecular dynamics simulations and density functional theory (DFT) calculations.

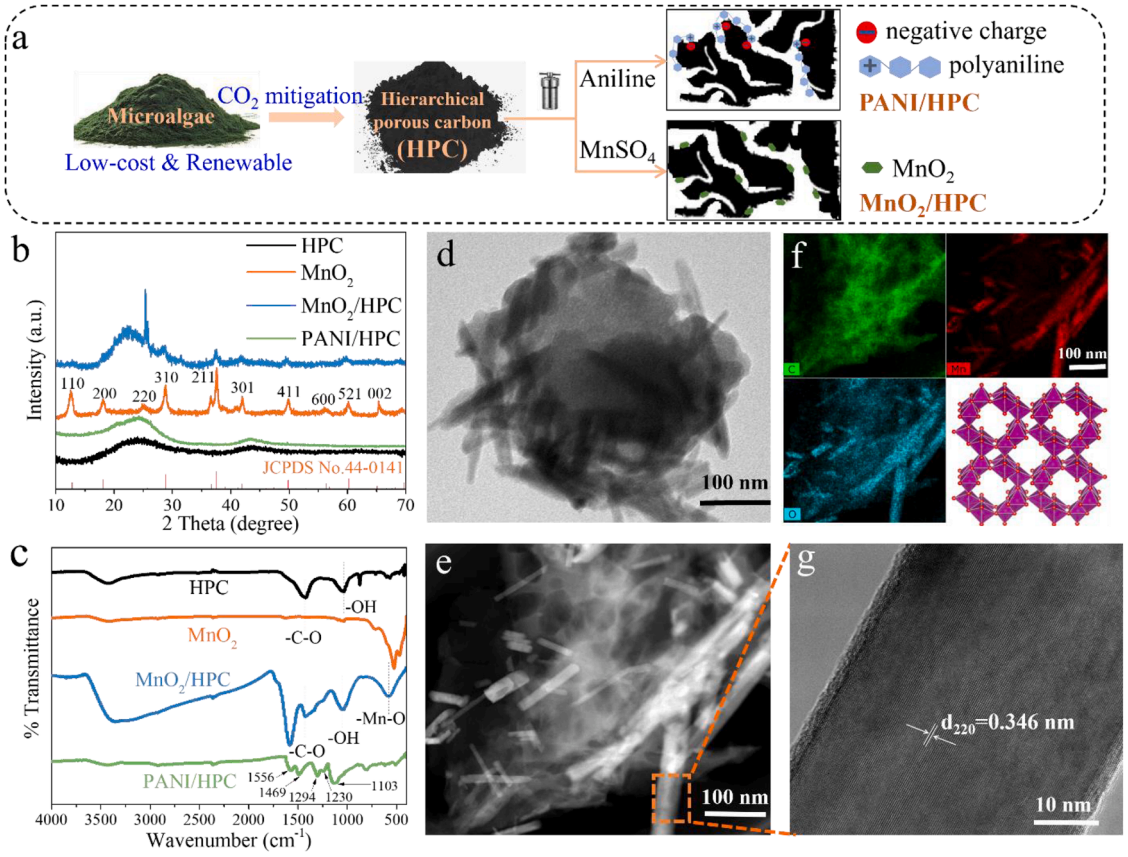

Fig. 1. (a) Schematic illustration of the preparation of the MnO_2/HPC and PANI/HPC; (b) XRD patterns of the HPC, MnO_2, MnO_2/HPC and PANI/HPC; (c) FTIR spectra of the HPC, MnO_2, MnO_2/HPC and PANI/HPC; (d) TEM image of the MnO_2/HPC; (e) HAADF-STEM image of the MnO_2/HPC; (f) HAFFD elemental mapping on the MnO_2/HPC of C, Mn, O, and the crystal structure of α-MnO_2 (derived from VESTA); (g) HAADF-STEM image showing the (220) lattice plane of a single MnO_2.

2. Results and discussion

2.1. Preparation and characterizations of the electrodes

The facile preparation procedure of the MnO_2/HPC and PANI/HPC is illustrated in Fig. 1a. The X-ray diffraction (XRD) pattern of MnO_2 confirms the formation of α-MnO_2 (JCPDS No. 44–0141) (Fig. 1b) (Leong and Yang, 2019). Similarly, three peaks centered at 37.1°, 41.8°, and 66.3° were clearly observed, which could be attributed to the (211), (301) and (002) planes of α-MnO_2. In contrast, both HPC and PANI/HPC showed an amorphous structure, as two broad peaks at 24.0° and 43.8° were observed (Fig. 1b). Raman spectra of the HPC and MnO_2/HPC show G and D bands at 1595 and 1333 cm^{-1}, respectively, indicating ordered graphene and disordered amorphous carbon structures (Fig. S1) (Evans et al., 2019). In addition, multiple features in the fingerprint region (1556, 1469, 1295, 1230 and 1103 cm^{-1}) were observed in the Fourier transform infrared (FTIR) pattern of the PANI/HPC, which resulted from the different aromatic modes in the PANI polymer (Fig. 1c). More importantly, the feature at 1103 cm^{-1} demonstrates the presence of the conducting form of PANI on the surface of HPC, and the feature at approximately 511 cm^{-1} proves the existence of Mn-O on the MnO_2/HPC composite surface (Evans et al., 2019; Tan et al., 2021). The transmission electron microscopy (TEM) images of the MnO_2/HPC and PANI/HPC clearly show that both MnO_2 and PANI were formed on the HPC surface, respectively (Fig. 1d and Fig. S2). Specifically, the α-MnO_2 samples show typical nanowire bundles (Fig. 1e). The elemental mapping of the MnO_2/HPC indicates the presence of Mn and O elements (Fig. 1f), exhibiting the uniform distribution of Mn and O in the MnO_2/HPC. The D-spacing is approximately 0.346 nm, which corresponds to the (220) crystal plane of the α-MnO_2 structure (Fig. 1g). In addition, scanning electron microscopy (SEM) images further demonstrate that the MnO_2 nanorods were uniformly formed on the HPC surface (Fig. S3).

A new peak of Mn 2p was observed in the X-ray photoelectron spectroscopy (XPS) spectrum of the MnO_2/HPC, and two new peaks of N 1 s and Cl 2p were observed in the PANI/HPC (Fig. S4). The high-resolution XPS spectra of the MnO_2/HPC in the Mn 2p region presented two peaks at 653.7 eV (Mn 2p1/2) and 642.0 eV (Mn 2p3/2), indicating that the oxidation state of Mn was +4 (Fig. S5) (Chong et al., 2018). The high-resolution XPS spectra of the PANI/HPC in the N 1 s region (~ 400 eV) confirm the presence of N (-NH- and -*N*=) from PANI (Fig. S6) (Evans et al., 2019). In addition, the PANI/HPC had a positive zeta potential of 15.7 mV, indicating that it could selectively absorb negative ions like Cl^- (Fig. S7). Conversely, both MnO_2 (−20.7 mV) and MnO_2/HPC (−23.9 mV) exhibited negative zeta potentials, implying that they could selectively absorb positive ions such as Na^+, Mg^{2+} and Ca^{2+} via electrostatic force. The hydrophilicity of the electrodes was evaluated by static water contact angles (Fig. S8). Compared to the HPC and MnO_2 electrodes, both MnO_2/HPC and PANI/HPC electrodes exhibited smaller water contact angles, suggesting that they were readily wetted and accessed by the salty solution (Tan et al., 2021).

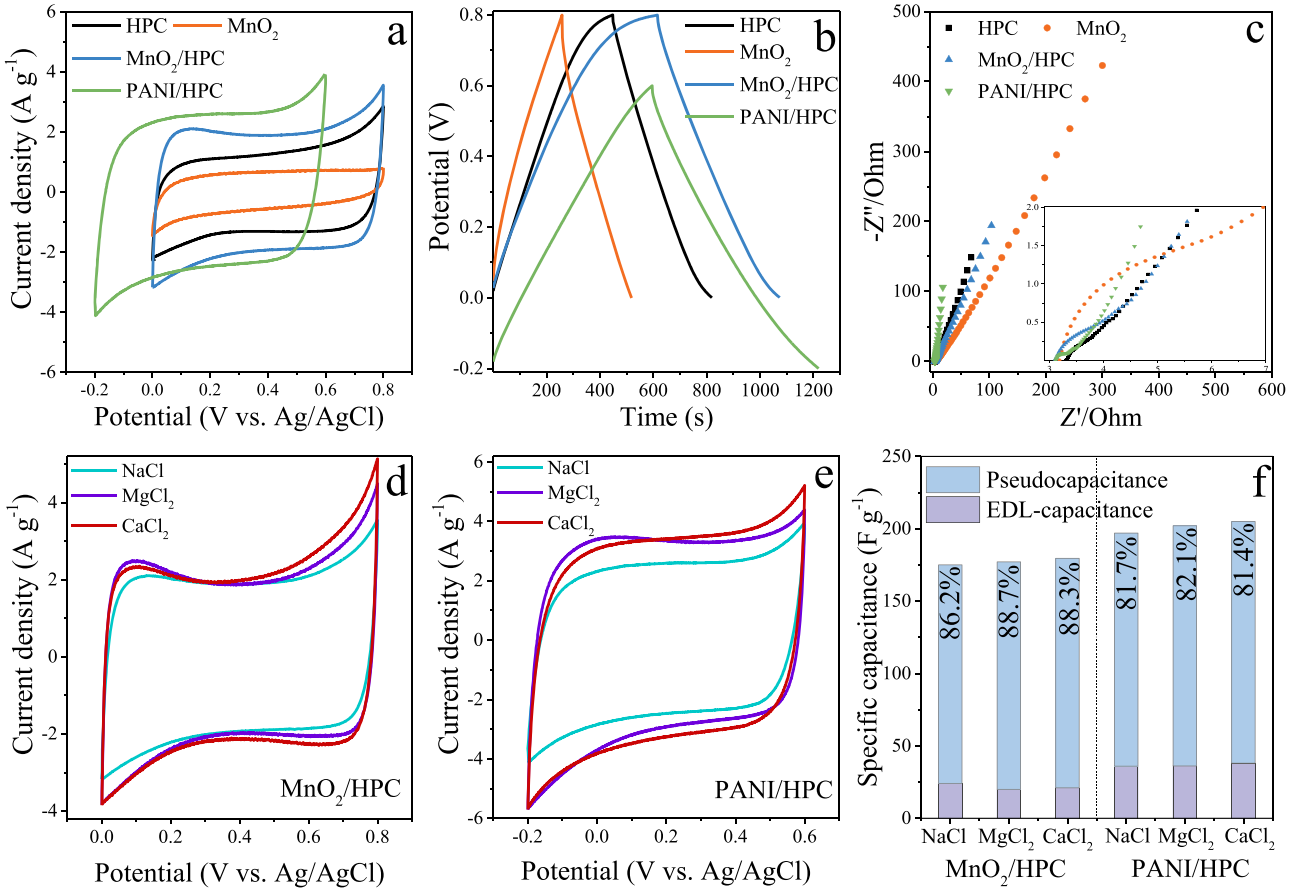

Fig. 2. (a) Cyclic voltammograms of the HPC, MnO_2, MnO_2/HPC and PANI/HPC electrodes at a scan rate of 5 mV s^{-1} in 1 M NaCl solution; (b) Representative galvanostatic charge/discharge profiles of the HPC, MnO_2, MnO_2/HPC and PANI/HPC electrodes in 1 M NaCl solution at a current density of 0.3 A g^{-1}; (c) Nyquist plots for the impedance responses of the HPC, MnO_2, MnO_2/HPC and PANI/HPC electrodes (inset shows a close-up of the near origin section) in 1 M NaCl solution; (d) Cyclic voltammograms of the MnO_2/HPC electrode at a scan rate of 5 mV s^{-1} in 1 M NaCl, $MgCl_2$ and $CaCl_2$ solutions; (e) Cyclic voltammograms of the PANI/HPC electrode at a scan rate of 5 mV s^{-1} in 1 M NaCl, $MgCl_2$ and $CaCl_2$ solutions; and (f) Pseudocapacitance and EDL capacitance contributions to the specific capacitances of the MnO_2/HPC and PANI/HPC electrodes in 1 M NaCl, $MgCl_2$ and $CaCl_2$ solutions.

2.2. Electrochemical performance of the electrodes

Similar to the HPC electrode, the MnO_2, MnO_2/HPC and PANI/HPC electrodes depicted rectangular-shaped voltammograms (Fig. 2a; and Fig. S9). These cyclic voltammetry (CV) curves were consistent with the previous reports on MnO_2@carbon and PANI@carbon composite electrodes, indicating their pseudocapacitive behaviors (Evans et al., 2019). Both MnO_2/HPC and PANI/HPC electrodes exhibited larger responsive currents, suggesting their higher specific capacitances. Their charge–discharge profiles in 1 M NaCl solution further confirm their pseudocapacitive behaviors with symmetric and linear curves (Fig. 2b and Fig. S10). In line with the CV results, the PANI/HPC electrode possessed the largest specific capacitance of 197.1 F g^{-1}, followed by the MnO_2/HPC (175.2 F g^{-1}), HPC (153.9 F g^{-1}), and MnO_2 (102.4 F g^{-1}) electrodes at 0.3 A g^{-1} (Fig. S11). The higher specific capacitances in the MnO_2/HPC electrode was attributed to the synergistic effects between the HPC and MnO_2. Because the porous HPC serves as a supportive backbone in the MnO_2/HPC composite, which could prevent the particle aggregation and reduce the volume expansion-contraction of MnO_2 (Chen et al., 2013; Jia et al., 2018). Besides, the faradaic pseudocapacitance from the MnO_2 can further improve the specific capacitance of MnO_2/HPC. Since the conductive PANI layer on the surface of HPC could facilitate easy and fast ion transportation, the PANI/HPC electrode had the smallest R_{ct} (0.23 Ω) and σ (12.36 Ω $s^{0.5}$) values (Table S1, Fig. 2c and Fig. S12). In comparison with the poor conductivity in the MnO_2 electrode (R_{ct} = 2.76 Ω, σ = 44.88 Ω $s^{0.5}$), the MnO_2/HPC also had much lower R_{ct} (0.23 Ω) and σ (12.36 Ω $s^{0.5}$) values. The well-dispersed MnO_2 nanorods connected with the conductive matrix of HPC could substantially facilitate the ion and electron transportation (Fig. S3) (Chen et al., 2013; Sevilla et al., 2017).

Similarly, the quasi-rectangular shape in the CV curves was also observed for the MnO_2/HPC and PANI/HPC electrodes in 1 M $MgCl_2$ and $CaCl_2$ electrolytes with a slightly higher current response compared to that of 1 M NaCl (Fig. 2d and 2e). Consistent with the CV results, the galvanostatic charge/discharge curves of the MnO_2/HPC electrode in 1 M $MgCl_2$ and $CaCl_2$ electrolytes also showed linear and symmetric curves, but had relatively higher specific capacitances of 177.3 F g^{-1} ($MgCl_2$) and 179.6 F g^{-1} ($CaCl_2$), respectively (Fig. S13). Similarly, the MnO_2@carbon electrode was reported to have a similar specific capacitance in equimolar concentrations of NaCl and $MgCl_2$ electrolytes (Xu et al., 2021). The relatively higher specific capacitances of the MnO_2/HPC and PANI/HPC electrodes in divalent electrolytes (i.e., $MgCl_2$ and $CaCl_2$) also indicate their excellent water softening capacity. Then, Dunn's method (Fig. S14) (Tan et al., 2021) was used to calculate the contributions of EDL capacitance and pseudocapacitance for the MnO_2/HPC and PANI/HPC electrodes, respectively. As shown in Fig. 2f, the approximately 87% capacitance of the MnO_2/HPC electrode resulted from pseudocapacitance, and the capacitance was approximately 82% for the PANI/HPC electrode in 1 M NaCl, $MgCl_2$ and $CaCl_2$ electrolytes. These results further demonstrate that the pseudocapacitive intercalation process was the main charge-storage mechanism in the electrochemical reaction for both MnO_2/HPC and PANI/HPC electrodes in NaCl, $MgCl_2$ and $CaCl_2$ electrolytes. More importantly, the pseudocapacitive-contributed capacities in the hardness ion electrolytes ($MgCl_2$ and $CaCl_2$) were relatively higher than those in the NaCl electrolyte.

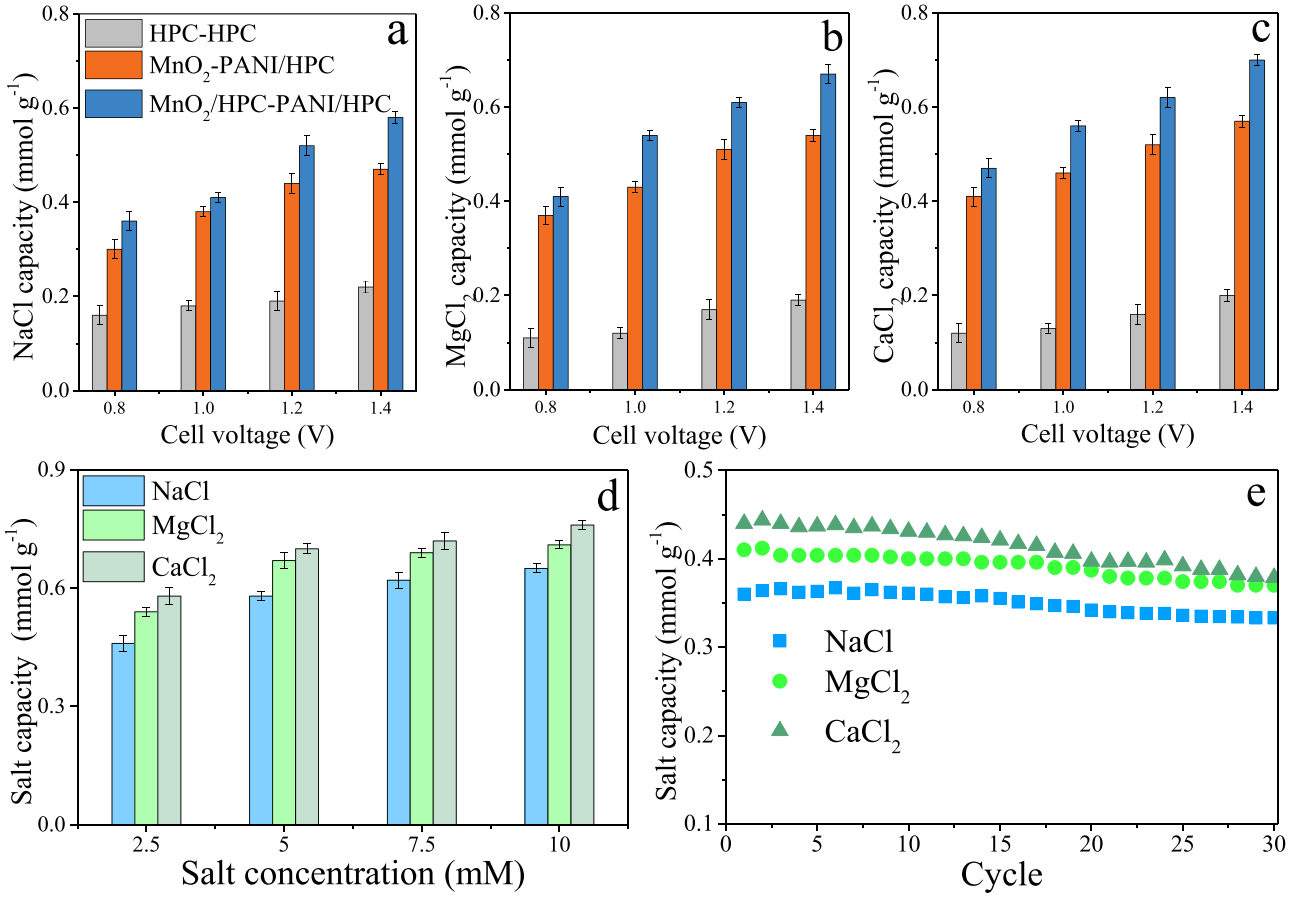

Fig. 3. Salt electrosorption capacities of the HPC—HPC, MnO_2-PANI/HPC and MnO_2/HPC-PANI/HPC cells in 5 mM (a) NaCl, (b) $MgCl_2$ and (c) $CaCl_2$ single salt solutions at different applied cell voltages; (d) Salt electrosorption capacities of the MnO_2/HPC-PANI/HPC cells in different feed concentrations of NaCl, $MgCl_2$ and $CaCl_2$ single salt solutions at ±1.4 V; (e) Cycling performance of the MnO_2/HPC-PANI/HPC cell in 10 mM NaCl, $MgCl_2$ and $CaCl_2$ solutions over 30 cycles at ±0.8 V.

2.3. Water desalination and water softening performance

The representative current density and NaCl concentration profiles of the HPC—HPC, MnO_2-PANI/HPC and MnO_2/HPC-PANI/HPC cells are depicted in Fig. S15. At each applied cell voltage, the MnO_2/HPC-PANI/HPC cell always possessed the highest salt electrosorption capacity, followed by the MnO_2-PANI/HPC and HPC—HPC cells (Fig. 3a-3c). Fig. S16 shows the corresponding average salt electrosorption rates, charge efficiencies and energy consumptions. Obviously, the best desalination performance was observed for the MnO_2/HPC-PANI/HPC cell. The energy consumption for the MnO_2/HPC-PANI/HPC cell in 5 mM NaCl solution was only 0.64 Wh g^{-1}, which was considerably lower than previously reported conventional CDIs as well as MnO_2-based hybrid CDIs (Hand and Cusick, 2017; He et al., 2021; Xu et al., 2021). Notably, only 0.17 Wh L^{-1} of energy was required to desalinate the feed solution to drinking water (<20 mg L^{-1} NaCl), making it quite low compared to RO processes (0.5 − 2.5 Wh L^{-1} for brackish water with salinity <10 g L^{-1}) (Tan et al., 2020; Zhao et al., 2013). The highest electrosorption capacities for the MnO_2/HPC-PANI/HPC cell was up to 0.65 mmol g^{-1} NaCl, 0.71 mmol g^{-1} $MgCl_2$ and 0.76 mmol g^{-1} $CaCl_2$ (Fig. 3d). Its maximum NaCl electrosorption capacity was comparable and even higher than the values reported in the previous studies (Table S2), in which similar MnO_2 or MnO_2(PANI)@carbon composite electrodes were applied (Jin et al., 2020; Nie et al., 2020). In addition, the maximum $MgCl_2$ and $CaCl_2$ electrosorption capacities were also higher than those in the previous reports (Table S3-S4) (Liu et al., 2020; Uwayid et al., 2022). Its excellent brackish water desalination and water softening performance could mainly be ascribed to the pseudocapacitive behaviors of the PANI/HPC and MnO_2/HPC electrodes, which can selectively intercalate negative ions (Cl^-) and positive ions (Na^+, Mg^{2+} and Ca^{2+}) (Evans et al., 2019; Tan et al., 2020; Wang et al., 2019). In addition, the synergistic effects between the high porosity of the HPC and MnO_2 (PANI) could generate higher specific capacitances, better hydrophilicity and reduce charge transfer and ionic diffusion resistances, thereby guaranteeing excellent desalination performance (Fig. 2 and Fig. S8).

Then, the cycling performance of the MnO_2/HPC-PANI/HPC cell was examined. The NaCl electrosorption capacity remained at approximately ca. 0.35 mmol g^{-1}, the $MgCl_2$ electrosorption capacity remained at ca. 0.39 mmol g^{-1}, while the $CaCl_2$ electrosorption capacity was stable at ca. 0.42 mmol g^{-1} (Fig. 3e). In addition, the desorption efficiency remained approximately 96%, suggesting that the MnO_2/HPC-PANI/HPC cell exhibited exceptional regeneration capabilities (Fig. S17). The porous HPC served as a supportive backbone in the MnO_2/HPC composite, which could prevent particle aggregation, reduce the volume expansion-contraction of MnO_2, enhance the structural integrity and perform long-term cycling (Chen et al., 2013). In order to further illustrate the stability, the MnO_2/HPC powder was scratched off from the carbon cloth for Raman, XRD, SEM and TEM characterizations. The intensity ratio of D-band to G-band (I_D/I_G) increased from 0.99 to 1.02 after 30 cycles, indicating slight oxidation of the MnO_2/HPC electrode (Fig. S18). However, the XRD characterizations indicate that the crystal structure of the MnO_2/HPC electrode had no obvious change in comparison with the original one after 30 cycles in 10 mM NaCl (Fig. S19). There was also no significant change in the morphology of the MnO_2/HPC electrode (Fig. S20 and Fig. S21). In addition, the uniform coating of the PANI on the HPC surface could reduce the kinetics of parasitic reactions of carbon materials (Fig. S3). Additionally, the shallow traps for the PANI molecules in the pores of HPC can protect it from degradation (Evans et al., 2019; Gao et al., 2022). As a result, the PANI/HPC composite electrode could also retain a large cycling capacity (Evans et al., 2019). The galvanostatic charge/-discharge tests also demonstrated the high stability of the MnO_2/HPC and PANI/HPC electrodes (Fig. S22). Additionally, the effluent pH in 10 mM NaCl in all 30 cycles slightly decreased and stabilized at approximately 6.5~7.0 (Fig. S23). These results further demonstrate that the facile designed MnO_2/HPC could be applied as an efficient electrode material for improved brackish water desalination and hardness ion removal.

2.4. Cation selectivity of the α-MnO_2/HPC electrode

The cation selectivity of the MnO_2/HPC electrode in binary salt solutions was subsequently investigated (Fig. 4). The difference in cation electrosorption capacity between $Na^+$and Mg^{2+} cations gradually increased when the applied voltage was increased from 0.8 V to 1.4 V (Fig. 4a). Similar results were observed in the binary NaCl/$CaCl_2$ solution (Fig. 4b), indicating that the MnO_2/HPC possessed divalent selectivity over monovalent cations. Since the MnO_2/HPC surface was negatively charged (Fig. S7), there was a strong electrostatic force between divalent cations and the MnO_2/HPC surface (Leong and Yang, 2020; Leong et al., 2021). In addition, the active sites occupied by Na^+ could be gradually replaced by divalent cations (Mg^{2+} or Ca^{2+}) because of the stronger interaction between the divalent ions and the negatively charged electrode surface, which results from the ion-swapping effect (Srimuk et al., 2020; Xu et al., 2021). More importantly, the divalent cation selectivity could still be maintained when the concentration of $Na^+$was twice that of Ca^{2+} (Fig. S24), suggesting that the MnO_2/HPC electrode had a great potential in water softening. In addition, the MnO_2/HPC electrode showed a relatively higher affinity for Ca^{2+}than Mg^{2+} (Fig. 4c). One reason could be the slower kinetics of Mg^{2+} intercalation/deintercalation into the tunnel structure of α-MnO_2 than that of Ca^{2+}, as the hydrated ionic radius of Mg^{2+} (0.43 nm) is larger than that of Ca^{2+} (0.41 nm) (Singh et al., 2021; Shocron et al., 2022). The relatively higher hydration energy of Mg^{2+} (−1830 kJ mol^{-1}) compared to that of Ca^{2+} (−1505 kJ mol^{-1}) could also limit Mg^{2+} intercalation/deintercalation (Fig. 4d and e). Other studies also showed that Ca^{2+} could be more strongly attracted to the negatively charged electrode because of its smaller hydrated radius compared to that of Mg^{2+} (Singh et al., 2021).

To further evaluate the selective capacity of Mg^{2+} and Ca^{2+} over Na^+ in the MnO_2/HPC electrode, the intercalation mechanisms were elucidated using molecular dynamics simulations and DFT calculations. The intercalation capacities of cations in the MnO_2/HPC were evaluated by Monte Carlo simulations. The results indicate that the amount of Mg^{2+} and Ca^{2+} was obviously greater than that of Na^+ (Fig. 5a and b). This might be attributed to the relatively higher binding energy between divalent cations and the electrode than that of Na^+ (Fig. 5c) (DuChanois et al., 2022). The cation selectivity of the MnO_2/HPC was largely dependent on the special configuration of α-MnO_2. In addition, the interaction energies (ΔE_{inter}) of cations and α-MnO_2 were precisely examined by DFT calculations through the unit cell model of α-MnO_2. For the limited lumen size, only one water molecule can be encapsulated in the cavity with the cation after equilibrium (Fig. S25 and Fig. 5d-f). The location site of the cations is offset from the center of the cavity of α-MnO_2 (Table S5). From the ΔE_{inter} of the cations in α-MnO_2 (Fig. 5g), it is obvious that the binding strength of Mg^{2+} and Ca^{2+} to the lumen side is much higher than that of Na^+. This proves that the intercalation selectivity of divalent cations in the electrode can be contributed by the stronger binding strength of Mg^{2+} and Ca^{2+} in the cavity of α-MnO_2 (Singh et al., 2021). Moreover, the charge distributions of the cation intercalation systems from Mulliken charge analysis indicate that only 0.44|e| electrons are transferred from α-MnO_2 and H_2O to Na^+ (Table S6), while 0.76|e| and 0.82|e| are transferred from that to Mg^{2+} and Ca^{2+}, respectively. The electron density difference also confirms the direction and degree of electron transfer in the encapsulation of cations to α-MnO_2 (Fig. 5d-f and Fig. S26) (Su et al., 2018). Thus, the MnO_2/HPC electrodes with a reasonable combination and configuration offer better intercalation selectivity of Mg^{2+} and Ca^{2+}. Overall, the MnO_2/HPC electrode exhibited a selectivity order of $Ca^{2+} \geq Mg^{2+} > Na^+$ due to the differences in valence, hydrated radius and binding strength in the cavity of MnO_2.

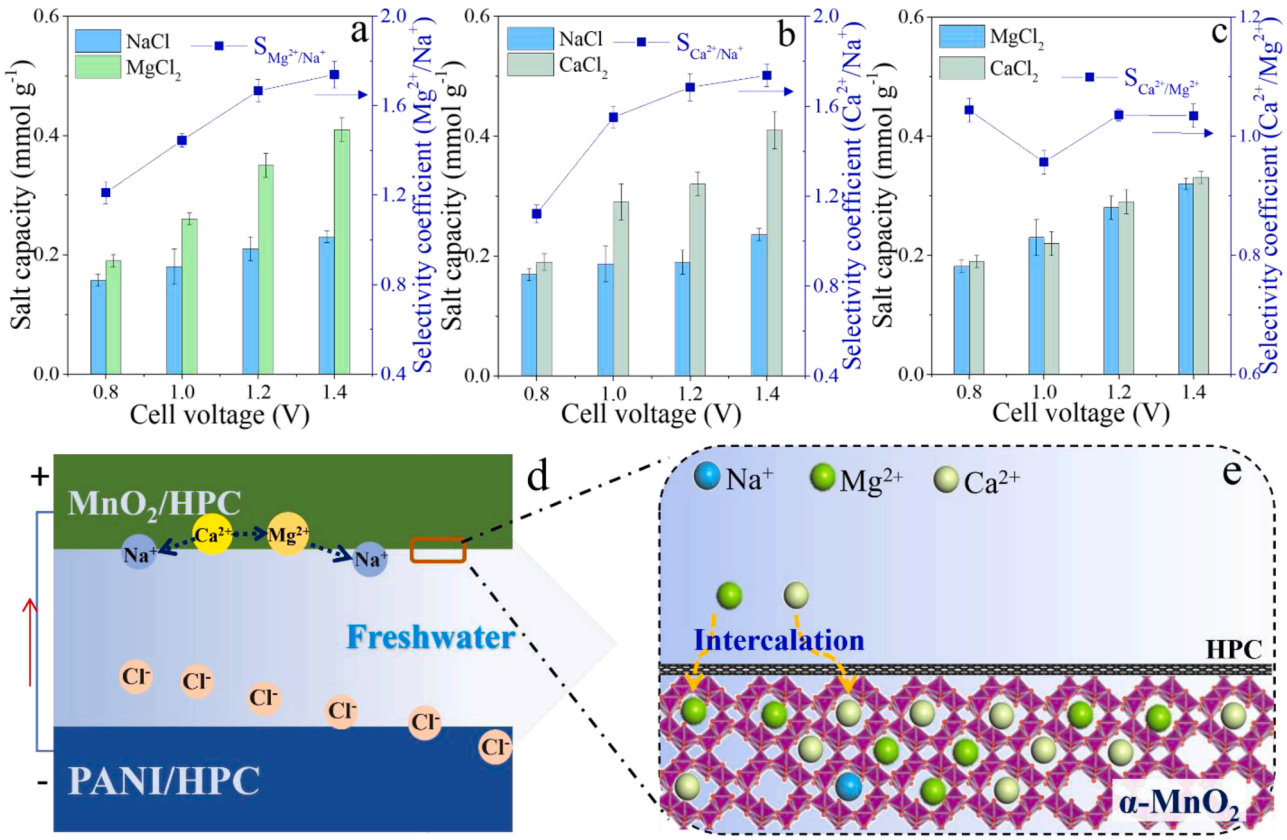

Fig. 4. Salt electrosorption capacities and selectivity coefficients of the MnO_2/HPC-PANI/HPC cells in binary salt solutions containing (a) 5 mM NaCl and 5 mM MgCl2; (b) 5 mM NaCl and 5 mM $CaCl_2$, and (c) 5 mM $MgCl_2$ and 5 mM $CaCl_2$; (d) Schematic of the MnO_2/HPC-PANI/HPC CDI cell. (e) The possible pathway for cation selectivity of Na^+, Mg^{2+} and Ca^{2+} ions by the MnO_2/HPC electrode.

3. Conclusions

The well-dispersed MnO_2 nanorods connected with HPC were prepared using a facile, one-step hydrothermal approach. The prepared MnO_2/HPC electrode had a considerable specific capacitance of 175.2 F g^{-1}, low charge transfer and ion diffusion resistance, and superior stability. In comparison with the HPC—HPC and MnO_2-PANI/HPC cells, the MnO_2/HPC-PANI/HPC cell exhibited the highest NaCl, $MgCl_2$ and $CaCl_2$ electrosorption capacity, fastest salt electrosorption rate, highest charge efficiency and lowest energy consumption. The MnO_2/HPC electrode delivered selective intercalation to the hardness ions ($Mg^{2+}$and Ca^{2+}) in the binary salt solutions. Both ion valence and radius could affect their competitive intercalation into the MnO_2/HPC electrode. Furthermore, molecular dynamics simulations and DFT calculations indicate that the preference of MnO_2/HPC toward divalent ions was mainly due to their stronger binding strength in the cavity of MnO_2. Our results clearly demonstrate that CDI with the facile designed MnO_2/HPC composite electrode can offer a great promise in brackish water desalination and water softening.

4. Material and methods

4.1. Preparation of MnO_2/HPC and polyaniline/HPC

The chemicals used in this work are described in the Supporting Information. The HPC was produced from microalgae (*Spirulina platensis*) biomass (Sevilla et al., 2017). First, the microalgae samples were thoroughly mixed with $CaCO_3$ and $K_2C_2O_4$ (at a weight ratio of 1:0.5:0.5) in an Agatha mortar, pyrolyzed in a tube furnace in a N_2 environment and held at 800 °C for 2 h. The obtained HPC powders were soaked and washed with 0.1 M HCl several times to remove inorganic impurities and then thoroughly washed with deionized water. Then, both MnO_2/HPC and PANI/HPC were prepared via a facile, one-step hydrothermal procedure (Fig. 1a) (Evans et al., 2019). For the MnO_2/HPC, 0.35 g $MnSO_4$, 1 g $K_2S_2O_8$ and 0.35 g HPC powder were mixed in 56 mL deionized water (DI) under stirring for 20 min at room temperature. Then, 4 mL KOH (1 M) was wisely dropped into the solution with magnetic stirring for an additional 30 min. The obtained mixture was transferred into a 100 mL Teflon-lined stainless-steel autoclave, which was heated for 12 h at 110 °C in an electric oven. Later, the produced precipitates were washed with DI water several times and collected by vacuum filtration. MnO_2 was produced with the same procedure without the addition of HPC. For the PANI/HPC, 0.35 g HPC powder, 0.35 g aniline and 3 mL HCl (37%) were added into 55 mL DI water with magnetic stirring for 6 h at 4 °C. Then, 2 g ammonium persulfate was added to the solution with magnetic stirring for an additional 2 h at 4 °C. Similarly, the obtained mixture was transferred into a 100 mL Teflon-lined stainless-steel autoclave and heated for 6 h at 120 °C. The formed PANI/HPC was then washed with DI water and ethanol several times and collected by vacuum filtration. Finally, the MnO_2, MnO_2/HPC and PANI/HPC samples were dried in vacuum at 50 °C for 24 h. Details about the preparation and characterizations of the HPC, MnO_2, MnO_2/HPC and PANI/HPC electrodes are given in the Supporting Information.

4.2. Capacitive deionization tests

The desalination of brackish water (2.5–10 mM NaCl) and softening of water (2.5–10 mM $MgCl_2$ and $CaCl_2$) were performed in a homemade CDI cell (Fig. S27). The cell consisted of a cathode (HPC or PANI/HPC) and an anode (HPC, MnO_2 or MnO_2/HPC). The water channel was formed by a 0.5 mm thick silicon gasket between the anode and cathode,

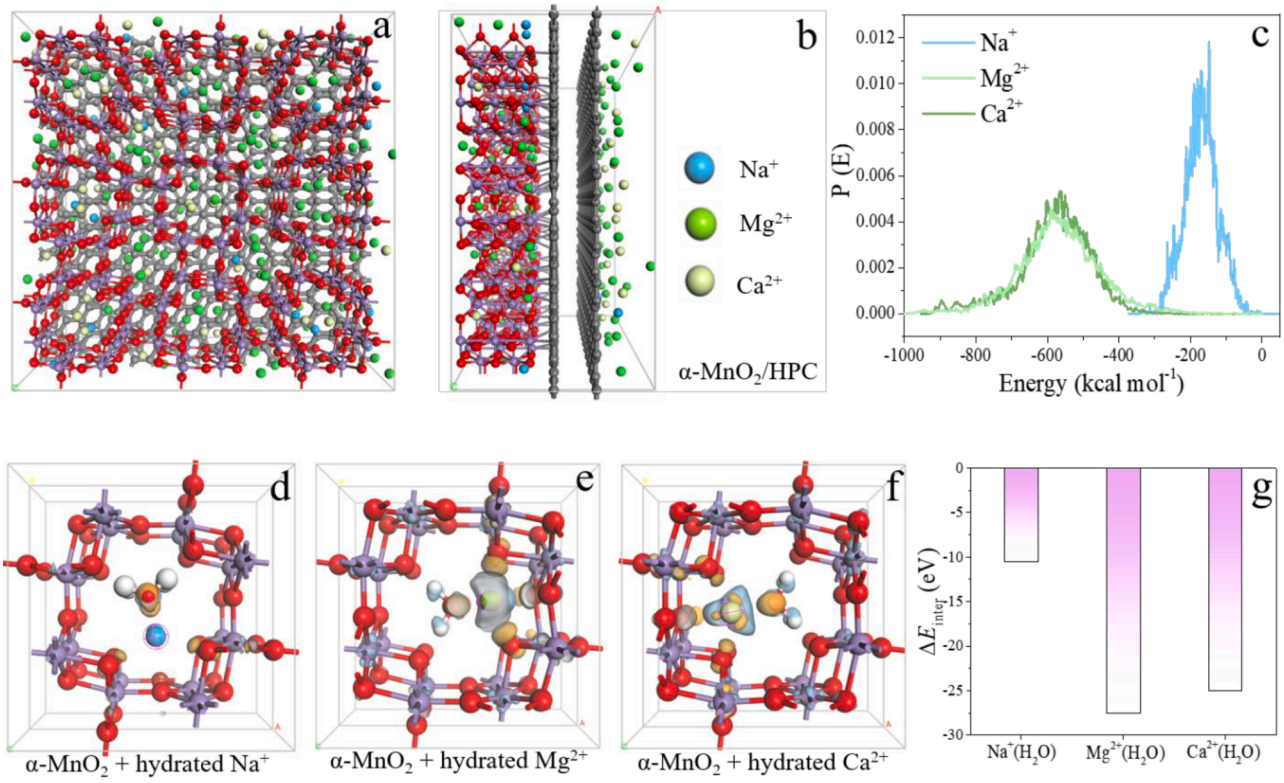

Fig. 5. Grand canonical Monte Carlo (GCMC) simulation results of Na^+, Mg^{2+} and Ca^{2+} intercalation into the MnO_2/HPC from the top view (a) and side view (b); (c) Energy density distributions for Na^+, Mg^{2+} and Ca^{2+} intercalation on MnO_2/HPC; Electron density distributions of MnO_2 with intercalated hydrated Na^+ (d), Mg^{2+} (e) and Ca^{2+} (f) from the top view. (Blue and yellow areas represent the increased and decreased electron densities, respectively, and the isosurface value is 0.05); (g) The intercalation energy of intercalated hydrated Na^+, Mg^{2+} and Ca^{2+} in the cavity of MnO_2.

and a filament fabric served as the spacer. Titanium foils were used as current leads. In the brackish water desalination and water softening processes, 70 mL of feed solution was circulated through the CDI cell at a flow rate of 35 mL min^{-1}. A constant voltage (i.e., ±0.8, ±1.0, ±1.2 V, or ±1.4 V) was applied to the cell by a potentiostat (PARSTAT MC, Princeton Applied Research Inc., USA). For the single salt solution, the concentration variation of ions was calculated according to the linear relationship between the concentration and conductivity, which was monitored by a conductivity meter (S230, Mettler Toledo, Co., Switzerland). For the binary salt solution, the concentration variation of ions was measured by an inductively coupled plasma atomic emission spectrometer (ICAP7400, Thermo Scientific, Inc., USA). The pH variation of the effluent solution was monitored by a pH meter (S210, Mettler Toledo, Co., Switzerland). Details on the calculations of salt electrosorption capacity, salt electrosorption rate, charge efficiency and energy consumption are provided in the Supporting Information.

4.3. *Theoretical calculations*

The intercalation behaviors of Na^+, Mg^{2+} and Ca^{2+} in MnO_2/HPC were determined according to the Metropolis Monte Carlo method (Metropolis et al., 1953). The α-MnO_2/HPC supercell consists of two graphene sheets with a MnO_2 layer with a size of 29.82 Å × 29.52 Å × 16.20 Å, showing Mn-C bonds between the graphene layer and α-MnO_2. The molecular dynamics simulations were implemented to predict the intercalation amounts of ions in the MnO_2/HPC supercell using *Universal* force fields. The Ewald summation was used to evaluate the electrostatic interactions with an accuracy of 1×10^{-4} kcal/mol. The atom-based summation was applied to assess the van der Waals interactions by using cubic spline truncation of a 15.5 Å cutoff distance and a 1.0 Å spline width. The location and the amounts of the ion species could be reflected in the simulations. To further investigate the interaction energy between ions and α-MnO_2, DFT calculations were employed and the details are given in the Supporting Information.

Declaration of Competing Interest

The authors declare that they have no known competing financial interests or personal relationships that could have appeared to influence the work reported in this paper.

Data availability

Data will be made available on request

Acknowledgements

This work was supported by the National Key Research and Development Program of China (2019YFC0408502), and the National Natural Science Foundation of China (52200074, 51821006, 52192684, and 52022093). The numerical calculations in this paper were performed on the supercomputing system in the Supercomputing Center of the University of Science and Technology of China.

References

Bhat, A.P., Reale, E.R., del Cerro, M., Smith, K.C., Cusick, R.D., 2019. Reducing impedance to ionic flux in capacitive deionization with Bi-tortuous activated carbon electrodes coated with asymmetrically charged polyelectrolytes. Water Res. X 3, 100027.

Caldera, U., Breyer, C., 2023. Afforesting arid land with renewable electricity and desalination to mitigate climate change. Nat. Sustain. 1, 1–13.

Cerón, M.R., Aydin, F., Hawks, S.A., Oyarzun, D.I., Loeb, C.K., Deinhart, A., Zhan, C., Pham, T.A., Stadermann, M., Campbell, P.G., 2020. Cation selectivity in capacitive

deionization: elucidating the role of pore size, electrode potential, and ion dehydration. ACS Appl. Mater. Interface 12 (38), 42644–42652.
Chen, L.F., Huang, Z.H., Liang, H.W., Guan, Q.F., Yu, S.H., 2013. Bacterial-cellulose-derived carbon nanofiber@MnO_2 and nitrogen-doped carbon nanofiber electrode materials: an asymmetric supercapacitor with high energy and power density. Adv. Mater. 25 (34), 4746–4752.
Chen, T.-.H., Cuong, D.V., Jang, Y., Khu, N.-.Z., Chung, E., Hou, C.-.H., 2022. Cation selectivity of activated carbon and nickel hexacyanoferrate electrode materials in capacitive deionization: a comparison study. Chemosphere 307, 135613.
Chong, S., Wu, Y., Liu, C., Chen, Y., Guo, S., Liu, Y., Cao, G., 2018. Cryptomelane-type MnO_2/carbon nanotube hybrids as bifunctional electrode material for high capacity potassium-ion full batteries. Nano Energy 54, 106–115.
DuChanois, R.M., Heiranian, M., Yang, J., Porter, C.J., Li, Q., Zhang, X., Verduzco, R., Elimelech, M., 2022. Designing polymeric membranes with coordination chemistry for high-precision ion separations. Sci. Adv. 8 (9), eabm9436.
Evans, S.F., Ivancevic, M.R., Wilson, D.J., Hood, Z.D., Adhikari, S.P., Naskar, A.K., Tsouris, C., Paranthaman, M.P., 2019. Carbon polyaniline capacitive deionization electrodes with stable cycle life. Desalination 464, 25–32.
Gamaethiralalage, J.G., Singh, K., Sahin, S., Yoon, J., Elimelech, M., Suss, M.E., Liang, P., Biesheuvel, P.M., Zornitta, R.L., De Smet, L., 2021. Recent advances in ion selectivity with capacitive deionization. Energy Environ. Sci. 14 (3), 1095–1120.
Gao, F., Li, X., Shi, W., Wang, Z., 2022. Highly selective recovery of phosphorus from wastewater via capacitive deionization enabled by ferrocene-polyaniline-functionalized carbon nanotube electrodes. ACS Appl. Mater. Interface 14 (28), 31962–31972.
Hand, S., Cusick, R.D., 2017. Characterizing the impacts of deposition techniques on the performance of MnO_2 cathodes for sodium electrosorption in hybrid capacitive deionization. Environ. Sci. Technol. 51 (20), 12027–12034.
He, C., Ma, J., Zhang, C., Song, J., Waite, T.D., 2018. Short-circuited closed-cycle operation of flow-electrode CDI for brackish water softening. Environ. Sci. Technol. 52 (16), 9350–9360.
He, Z., Liu, S., Lian, B., Fletcher, J., Bales, C., Wang, Y., Waite, T.D., 2021. Optimization of constant-current operation in membrane capacitive deionization (MCDI) using variable discharging operations. Water Res. 204, 117646.
Hussain, F., Shah, S.Z., Ahmad, H., Abubshait, S.A., Abubshait, H.A., Laref, A., Manikandan, A., Kusuma, H.S., Iqbal, M., 2021. Microalgae an ecofriendly and sustainable wastewater treatment option: biomass application in biofuel and bio-fertilizer production. A review. Renew. Sustain. Energy Rev. 137, 110603.
Jia, H., Cai, Y., Lin, J., Liang, H., Qi, J., Cao, J., Feng, J., Fei, W., 2018. Heterostructural graphene quantum dot/MnO_2 nanosheets toward high-potential window electrodes for high-performance supercapacitors. Adv. Sci. 5 (5), 1700887.
Jin, J., Li, M., Tang, M., Li, Y., Liu, Y., Cao, H., Li, F., 2020. Phase- and crystallinity-tailorable MnO_2 as an electrode for highly efficient hybrid capacitive deionization (HCDI). ACS Sustain. Chem. Eng. 8 (30), 11424–11434.
Juran, T.R., Young, J., Smeu, M., 2018. Density functional theory modeling of MnO_2 polymorphs as cathodes for multivalent ion batteries. J. Phys. Chem. C 122 (16), 8788–8795.
Leong, Z.Y., Yang, H.Y., 2019. A study of MnO_2 with different crystalline forms for pseudocapacitive desalination. ACS Appl. Mater. Interface 11 (14), 13176–13184.
Leong, Z.Y., Yang, H.Y., 2020. Capacitive deionization of divalent cations for water softening using functionalized carbon electrodes. ACS Omega 5 (5), 2097–2106.
Leong, Z.Y., Zhang, J., Vafakhah, S., Ding, M., Guo, L., Yang, H.Y., 2021. Electrochemically activated layered manganese oxide for selective removal of calcium and magnesium ions in hybrid capacitive deionization. Desalination 520, 115374.
Liu, T., Serrano, J., Elliott, J., Yang, X., Cathcart, W., Wang, Z., He, Z., Liu, G., 2020. Exceptional capacitive deionization rate and capacity by block copolymer–based porous carbon fibers. Sci. Adv. 6 (16), eaaz0906.
Metropolis, N., Rosenbluth, A.W., Rosenbluth, M.N., Teller, A.H., Teller, E., 1953. Equation of state calculations by fast computing machines. J. Chem. Phys. 21 (6), 1087–1092.
Nie, P., Yan, J., Zhu, G., Liu, J., 2020. Inverted hybrid-capacitive deionization with polyaniline nanotubes doped activated carbon as an anode. Electrochim. Acta 339, 135920.
Oliveira, C.Y.B., Oliveira, C.D.L., Prasad, R., Ong, H.C., Araujo, E.S., Shabnam, N., Gálvez, A.O., 2021. A multidisciplinary review of *Tetradesmus obliquus*: a microalga suitable for large-scale biomass production and emerging environmental applications. Rev. Aquacult. 13 (3), 1594–1618.
Oyarzun, D.I., Hemmatifar, A., Palko, J.W., Stadermann, M., Santiago, J.G., 2018. Ion selectivity in capacitive deionization with functionalized electrode: theory and experimental validation. Water Res. X 1, 100008.
Rizwan, M., Mujtaba, G., Memon, S.A., Lee, K., Rashid, N., 2018. Exploring the potential of microalgae for new biotechnology applications and beyond: a review. Renew. Sustain. Energy Rev. 92, 394–404.
Sevilla, M., Ferrero, G.A., Fuertes, A.B., 2017. One-pot synthesis of biomass-based hierarchical porous carbons with a large porosity development. Chem. Mater. 29 (16), 6900–6907.
Shocron, A.N., Roth, R.S., Guyes, E.N., Epsztein, R., Suss, M.E., 2022. Comparison of ion selectivity in electrodialysis and capacitive deionization. Environ. Sci. Technol. 9 (11), 889–899.
Singh, K., Li, G., Lee, J., Zuilhof, H., Mehdi, B.L., Zornitta, R.L., de Smet, L.C.P.M., 2021. Divalent ion selectivity in capacitive deionization with vanadium hexacyanoferrate: experiments and quantum-chemical computations. Adv. Funct. Mater. 31 (41), 2105203.
Singh, K., Qian, Z., Biesheuvel, P.M., Zuilhof, H., Porada, S., de Smet, L.C.P.M., 2020. Nickel hexacyanoferrate electrodes for high mono/divalent ion-selectivity in capacitive deionization. Desalination 481, 114346.
Srimuk, P., Su, X., Yoon, J., Aurbach, D., Presser, V., 2020. Charge-transfer materials for electrochemical water desalination, ion separation and the recovery of elements. Nat. Rev. Mater. 5 (7), 517–538.
Su, X., Kushima, A., Halliday, C., Zhou, J., Li, J., Hatton, T.A., 2018. Electrochemically-mediated selective capture of heavy metal chromium and arsenic oxyanions from water. Nat. Commun. 9 (1), 1–9.
Tan, G., Lu, S., Xu, N., Gao, D., Zhu, X., 2020. Pseudocapacitive behaviors of polypyrrole grafted activated carbon and MnO_2 electrodes to enable fast and efficient membrane-free capacitive deionization. Environ. Sci. Technol. 54 (9), 5843–5852.
Tan, G., Xu, N., Gao, D., Zhu, X., 2021. Facile designed manganese oxide/biochar for efficient salinity gradient energy recovery in concentration flow cells and influences of mono/multivalent ions. ACS Appl. Mater. Interface 13 (17), 19855–19863.
Uwayid, R., Guyes, E.N., Shocron, A.N., Gilron, J., Elimelech, M., Suss, M.E., 2022. Perfect divalent cation selectivity with capacitive deionization. Water Res. 210, 117959.
Wang, J., Tang, J., Ding, B., Malgras, V., Chang, Z., Hao, X., Wang, Y., Dou, H., Zhang, X., Yamauchi, Y., 2017. Hierarchical porous carbons with layer-by-layer motif architectures from confined soft-template self-assembly in layered materials. Nat. Commun. 8 (1), 15717.
Wang, S., Wang, G., Wu, T., Li, C., Wang, Y., Pan, X., Zhan, F., Zhang, Y., Wang, S., Qiu, J., 2019. Membrane-free hybrid capacitive deionization system based on redox reaction for high-efficiency NaCl removal. Environ. Sci. Technol. 53 (11), 6292–6301.
Xu, Y., Xiang, S., Zhou, H., Wang, G., Zhang, H., Zhao, H., 2021. Intrinsic pseudocapacitive affinity in manganese spinel ferrite nanospheres for high-performance selective capacitive removal of Ca^{2+} and Mg^{2+}. ACS Appl. Mater. Interface 13 (32), 38886–38896.
Zhang, C., Ma, J., Wu, L., Sun, J., Wang, L., Li, T., Waite, T.D., 2021. Flow electrode capacitive deionization (FCDI): recent developments, environmental applications, and future perspectives. Environ. Sci. Technol. 55 (8), 4243–4267.
Zhang, L., Mishra, D., Zhang, K., Perdicakis, B., Pernitsky, D., Lu, Q., 2020. Electrokinetic study of calcium carbonate and magnesium hydroxide particles in lime softening. Water Res. 186, 116415.
Zhao, R., Porada, S., Biesheuvel, P.M., van der Wal, A., 2013. Energy consumption in membrane capacitive deionization for different water recoveries and flow rates, and comparison with reverse osmosis. Desalination 330, 35–41.
Zhao, R., van Soestbergen, M., Rijnaarts, H.H.M., van der Wal, A., Bazant, M.Z., Biesheuvel, P.M., 2012. Time-dependent ion selectivity in capacitive charging of porous electrodes. J. Colloid Interf. Sci. 384 (1), 38–44.
Zhou, W., Wang, J., Chen, P., Ji, C., Kang, Q., Lu, B., Li, K., Liu, J., Ruan, R., 2017. Bio-mitigation of carbon dioxide using microalgal systems: advances and perspectives. Renew. Sustain. Energy Rev. 76, 1163–1175.